View metadata, citation and similar papers at core.ac.uk

brought to you by CORE

provided by Elsevier - Publisher Connector

Energy Conversion and Management 108 (2016) 181–189

Contents lists available at ScienceDirect

Energy Conversion and Management

journal homepage: www.elsevier.com/locate/enconman

Experimental and numerical investigation of ion signals in boosted HCCI combustion using cesium and potassium acetate additives

J. Hunter Mack *, Ryan H. Butt, Yulin Chen, Jyh-Yuan Chen, Robert W. Dibble

University of California at Berkeley, Berkeley, CA, United States

ARTICLE INFO

Article history:
Received 29 September 2015
Accepted 5 November 2015
Available online 18 November 2015

Keywords:
Homogeneous charge compression ignition
Ion sensing
Fuel additive
Internal combustion
Ethanol

ABSTRACT

A sparkplug ion sensor can be used to measure the ion current in a homogeneous charge compression ignition (HCCI) engine, providing insight into the ion chemistry inside the cylinders during combustion. HCCI engines typically operate at lean equivalence ratios (ϕ) at which the ion current becomes increasingly indistinguishable from background noise. This paper investigates the effect of fuel additives on the ion signal at low equivalence ratios, determines side effects of metal acetate addition, and validates numerical model for ionization chemistry. Cesium acetate (CsOAc) and potassium acetate (KOAc) were used as additives to ethanol as the primary fuel. Concentration levels of 100, 200, and 400 mg/L of metal acetate-in-ethanol are investigated at equivalence ratios of 0.08, 0.20, and 0.30. The engine experiments were conducted at a boosted intake pressure of 1.8 bar absolute and compared to naturally aspirated results. Combustion timing was maintained at 2.5° after top-dead-center (ATDC), as defined by the crank angle degree (CAD) where 50% of the cumulative heat release occurs (CA50). CsOAc consistently produced the strongest ion signals at all conditions when compared to KOAc. The ion signal was found to decrease with increased intake pressure; an increase in the additive concentration increased the ion signal for all cases. However, the addition of the metal acetates decreased the gross indicated mean effective pressure ($IMEP_g$), maximum rate of heat release (ROHR), and peak cylinder pressure. Experimental results were used to validate ion chemistry mechanisms for cesium and potassium using a single-zone numerical engine model.

© 2015 The Authors. Published by Elsevier Ltd. This is an open access article under the CC BY-NC-ND license (http://creativecommons.org/licenses/by-nc-nd/4.0/).

1. Introduction

An experimental and numerical investigation of how various metal acetate fuel additives influence the ion chemistry in a homogeneous charge compression ignition (HCCI) engine operating at boosted intake pressures is the primary objective of this study. Additionally, characterizing the effect of potassium acetate (KOAc) and cesium acetate (CsOAc) additives on engine performance is of interest. The boosted results are presented next to naturally aspirated operation as a means of comparison.

Homogeneous charge compression ignition (HCCI) engines combine characteristics of both diesel and spark-ignited engines, including a homogeneous mixture of fuel and air (similar to a spark-ignited engine) and compression ignition (like a diesel engine). HCCI engines typically operate at lean equivalence ratios ($\phi < 0.4$), producing a low flame temperature (<2000 K). Therefore oxides of nitrogen (NO_x) emissions, which are highly dependent on temperature, are significantly lower compared to traditional combustion methods [1]. Chemical kinetics largely dictate the burn rate and combustion process in HCCI engines, as the temperature rise caused by the compression process is used to produce thermal conditions in which the mixture of fuel and oxidizer autoignite.

A main advantage of HCCI is its ability to achieve efficiencies similar to diesel engines due to high compression ratios, the elimination of throttling losses, and shorter combustion durations [2]. In addition to the low NO_x emissions, HCCI engines also have lower particular matter (PM) emissions in comparison to spark-ignited (SI) and diesel engines. The lean dilute homogeneous air–fuel mixture, and thus the absence of a diffusion flame, contributes to the low PM emissions. Another distinct advantage of HCCI combustion is its ability to operate on a number of different fuels including gasoline [3], diesel [4], natural gas [5], ethanol [6], butanol [7], and many different blends [8–10].

There are also several challenges facing HCCI. Due to the nature of autoignition, the combustion event is quite rapid and can lead to very high rates of heat and pressure rise at higher equivalence ratios; this results in a high ringing intensity that can damage the engine, lower efficiencies, and an increase in some emissions.

* Corresponding author at: University of Massachusetts Lowell, Lowell, MA, United States. Tel.: +1 978 934 5766.
E-mail address: hunter_mack@uml.edu (J.H. Mack).

http://dx.doi.org/10.1016/j.enconman.2015.11.012
0196-8904/© 2015 The Authors. Published by Elsevier Ltd.
This is an open access article under the CC BY-NC-ND license (http://creativecommons.org/licenses/by-nc-nd/4.0/).

Nomenclature

BDC	Bottom Dead Center
CA50	crank angle at which 50% of the heat has been released
CI	compression ignition
CsOAc	cesium acetate
DME	Dimethyl Ether
EGR	Exhaust Gas Recirculation
HCCI	homogeneous charge compression ignition
$IMEP_g$	gross indicated mean effective pressure
KOAc	potassium acetate
LHV	Lower Heating Value
LTC	Low Temperature Combustion
LTHR	Low Temperature Heat Release
MON	Motor Octane Number
NO_x	oxides of nitrogen
PM	Particulate Matter
PRF	Primary Reference Fuel
ROHR	rate of heat release
RON	Research Octane Number
SI	Spark Ignition
TDC	Top Dead Center
TDI	Turbocharged Direct Injection
UHC	Unburned Hydrocarbons

Additionally, since HCCI engines operate at low equivalence ratios, their power output is also limited by the amount of fuel available to the engine. As a result of these limits, HCCI engines tend to have a narrow operating range [11]. However, boosted intake pressures (to increase power) [12], partial fuel stratification (to reduce the pressure rise rate) [13], and thermal stratification [14] are potential avenues to expand the operating range.

Relatively high levels of UHC and CO emissions are another issue for HCCI engines [15,16], primarily the result of two routes: (1) trapped fuel/air mixture in the crevice regions [17] and (2) cold boundary layers near the chamber surface [18]. The gases present in the chamber during the expansion stroke are relatively cold and the temperature is not high enough to fully oxidize the gases exiting the crevice region. In regards to the cold boundary layer, the mixture does not combust in these regions due to thermal quenching.

Lastly, controlling the autoignition event is one of the most difficult problems to solve in HCCI engines, as autoignition is primarily controlled by the chemical kinetics of the mixture. The driving reactions are very sensitive to intake temperature and in-cylinder composition. In SI engines, the spark initiates the combustion event; fuel injection timing initiates the combustion event in diesel engines. These methods offer a great deal of control over when combustion occurs. However, in HCCI engines, combustion timing is difficult to control due the autoignition process. In order to control combustion timing, one must accurately measure when the ignition event occurs. Different combustion timing measurement methods have been researched, including piezo-electric pressure transducers, microphones [19], torque sensors [20], and sparkplug ion sensors. This study evaluates the use of sparkplug ion sensors as a means of detecting the combustion event.

Ion sensors in engines have been used in a variety of ways, including for misfire and knock detection in SI engines [21–23] and flame detectors [24] in HCCI engines. The electrically conductive properties of a flame enable ion measurement since ions are an intermediate step in hydrocarbon combustion processes [25]. A sparkplug ion sensor measures the ion signal in the combustion chamber by applying a bias voltage to the sparkplug gap. The ion current signal is produced by ions generated during autoignition; these ions become the conductive carriers within the gap.

The chemi-ionization process shown by Eq. (1) drives the ion signal inside an engine [26]. Free electrons are drawn to the positively charged center electrode of the sparkplug, thus producing the ion signal which is measured by the electric circuitry and provides an indication of the combustion event.

$$CH + O \rightarrow CHO^{+} + e^{-} \tag{1}$$

Multiple factors can influence the generation of ions and electrons, and thus the ion signal. Intake pressure, location in the combustion chamber, electrode surface area, and fuel composition have all been shown to affect the ion signal [26–28]. Of particular interest to this study is the trend that boosted intake pressures suppress the ion signal for neat fuels. Additionally, leaner equivalence ratios result in lower in-cylinder temperatures and lead to decreased production of CH radicals (evident in Eq. (1)). This can further reduce the ion signal. At extremely lean conditions, the ion signal becomes indistinguishable from the background noise. Fuel additives have been shown to enhance the strength of the ion signal. A previous study showed that the addition of metal acetates improved the ion signal-to-noise ratio at naturally aspirated conditions [29]. This study includes additional metal acetates and expands the operating regime to include boosted intake pressures.

The addition of metal acetates to the primary fuel enhances the ion signal by increasing the electron concentration inside the combustion chamber. The metals, belonging to the alkali metal group, have different ionization potentials. The first ionization potential for potassium is 50,338 K and 45,119 K for cesium [30]. The Saha Equation, shown in Eq. (2), correlates the ionization potential, electron density, and temperature dependence of the reactions. N represents the respective species number densities, K_p is the equilibrium constant, P is the pressure, T is the temperature, and θ_{metal} is the ionization potential.

$$K_P = \frac{N_e^2}{N_{metal}} * \frac{P}{N_{total}} = \exp\left(-\frac{\theta_{metal}}{T}\right) \tag{2}$$

As such, lower electron concentrations are expected at lower gas temperatures. From a practical point of view, the authors are not suggesting that these particular additives are suitable or ideal candidates for use in production fuels and engines as a means to enhance the ion signal. The aim of this study is to understand the mechanisms behind ion signals in HCCI engines; the metal acetates investigated here provide valuable insight into the underlying principles.

2. Materials and methods

2.1. Engine specifications

The engine used in the experimental portion of this paper is a modified four-cylinder 1.9 L Volkswagen TDI engine. The engine specifications and operating conditions are listed in Table 1. A schematic of the experimental set-up is included in Fig. 1. In order to operate in a HCCI mode, the engine includes significant modifications: replacement of the stock deep-bowl pistons with relatively flat pistons to reduce heat transfer, modification of the glow plug holes to fit standard 10 mm spark plugs (the ion sensors), installation of in-cylinder quartz piezoelectric pressure transducers (AVL Model QH33D) in the direct fuel injector ports,

Table 1
Engine specifications and operating conditions.

Configuration	4 cylinder
Displacement	1.9 L
Compression ratio	17.0:1
Bore	79.5 mm
Stroke	95.5 mm
Connection rod length	144.0 mm
Fuel injection	Port fuel injection
Fuel pressure	45 PSI
Valves (intake, exhaust)	1, 1
Intake valve open (IVO)	2°CA BTDC
Intake valve close (IVC)	47.5°CA ABDC
Exhaust valve open (EVO)	47.5°CA BBDC
Exhaust valve close (EVC)	8°CA ATDC
Overlap	0°CA
Maximum valve lift	10 mm
Engine speed	1800 RPM
Volume BDC	504.72 cm^3
Volume TDC	29.69 cm^3

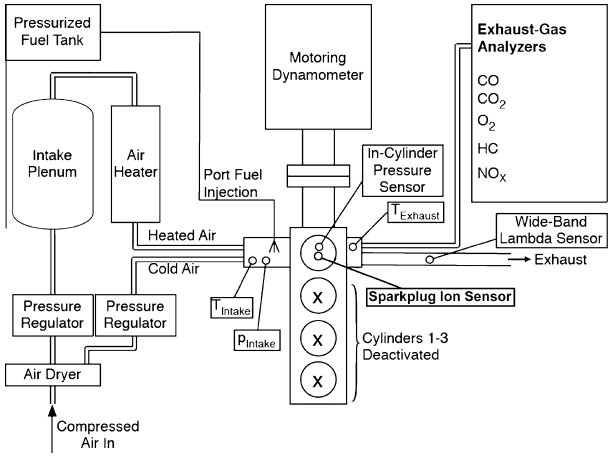

Fig. 1. Schematic of HCCI engine test bench, including intake system, and key diagnostic sensors.

design of a custom injection control system using solid-state relays and control signals generated from a National Instruments LabView program, use of a custom intake manifold including a port fuel injector system, monitoring of exhaust composition via wide-band lambda sensors, isolation of the cylinder 4 exhaust manifold to ensure accurate measurement of the equivalence ratio, replacing the turbocharger with an external 100 HP compressor (including a 6 m^3 surge tank) to achieve boosted intake conditions, measurement of intake pressure via a piezoresistive pressure sensor (Kulite XTEL 190 M) at crank-angle resolution, and temperature monitoring via multiple K-type thermocouples in the intake and exhaust manifolds.

Engine speed is controlled with an alternating current (AC) motor-generator connected to the engine using a direct-drive shaft and clutch. The engine speed is maintained at 1800 rpm at all times. Combustion timing is controlled by varying the intake temperature. Fig. 1 shows a schematic of the HCCI engine test bench and key sensors for the data acquisition and control. The engine has been converted to single-cylinder operation by deactivating cylinders 1–3. The configuration of the engine facility and data acquisition is similar to previous studies [29,31].

In-cylinder pressure is monitored using a pressure transducer connected to a charge amplifier. The pressure measurements are triggered by a crankshaft encoder with a resolution of 4 samples per crank angle degree. At each testing condition, 300 consecutive thermodynamic cycles are measured and recorded. The pressure data is used to calculate the heat release rate and indicated mean effective pressure. The most important recorded parameters for the controlling of the engine and the evaluation include intake pressure (p_{intake}), intake temperature (T_{intake}), in-cylinder pressure ($p_{in\text{-}cylinder}$), equivalence ratio (Φ), exhaust temperature ($T_{exhaust}$), coolant temperature ($T_{coolant}$), and oil temperature (T_{oil}). The coolant and oil temperature are kept in a constant range to guarantee comparable results during operation of the engine.

Fuel is port-injected in the intake manifold of cylinder 4 after mixing of the hot and cold air streams. The fuel injector is connected to a 12 volt battery through a solid-state relay, which provides control of the amount of fuel injected by varying the pulse width. The equivalence ratio is measured using wideband lambda sensors (Innovate Motorsports LC-1), located in the exhaust manifold of cylinder 4. The lambda sensors output an analog voltage proportional to the oxygen (or unburned fuel fraction) in the exhaust. The lambda sensor output is used to control the pulse width of the fuel injection event by a feedback control loop.

The crank angle at which 50% of the heat from combustion has been released (CA50) is calculated from the in-cylinder pressure data and monitored in real-time during testing. CA50 serves as a feedback parameter for adjusting the intake temperature T_{intake}, which is controlled by adjusting the intake air heater. Combustion timing is advanced as the intake temperature is increased. As shown in Fig. 1, the intake temperature is fine-tuned by adjusting the amount of mass flow of hot air and cold (ambient temperature) air. The amount of cold air is regulated via the pressure regulator installed upstream of the intake in the cold air supply.

2.2. Ion circuit design

A sparkplug ion sensor is used for measuring the ion signal using the center electrode as the positive bias [26]. Fig. 2 shows a schematic of the ion signal acquisition system, which has been used in a previous study [28]. A bias voltage of 237 V is applied across the sparkplug; the resultant voltage is measured across a 241 kΩ resistor.

During autoignition in the combustion chamber, an ion current is formed across the two biased electrodes of the unmodified spark plug. Prior to sampling, the signal is passed through a band-stop filter to smooth out signal noise. The filter specification is based on maximizing the signal strength and stability while minimizing the delay with respect to the start of combustion as measured by the pressure transducer. The active twin-T band-stop filter, with

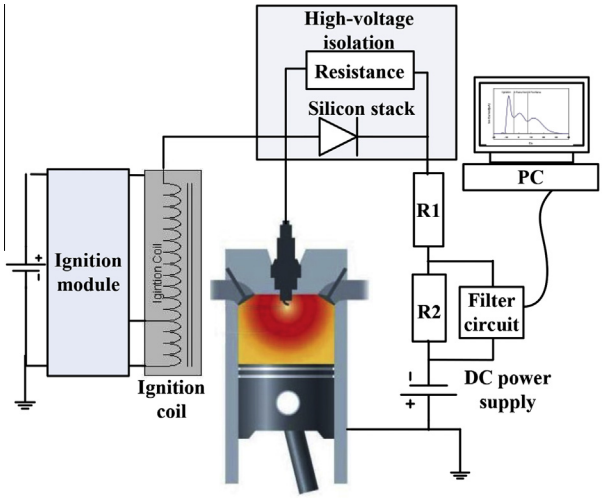

Fig. 2. Schematic of the ion signal acquisition system.

a roll-off rate of 40 dB/decade and a resonant frequency of 60.3 Hz, is also used to remove 60 Hz noise from the signal. The circuit additionally serves as an isolation circuit to protect the data acquisition system from any potential voltage spikes. Alternating current (AC) noise reduction is achieved by four capacitors installed as close as possible to the power supply pins on the breadboard for the operational amplifier.

2.3. Data acquisition and post-processing

The data was collected at stable, non-transient engine operating points with constant intake conditions (temperature, pressure, and equivalence ratio). Each test point was replicated for consistency in the results. The measured data of the experiments is post-processed to calculate the rate of heat release (ROHR) and the in-cylinder temperature profiles [31]. The average pressure trace, which serves as a basis for post-processing, is acquired using a Savitzky–Golay filter with 19 points [32] in conjunction with three hundred consecutive cycles. The ROHR model included heat loss from blow-by to the walls, defined using a Woschni model and using calibration factors determined from cycle simulation calculations [33,34]. Thermodynamic properties of the mixture are calculated using Lawrence Livermore National Laboratory (LLNL) and National Aeronautics and Space Administration (NASA) polynomials where it is assumed that the mixture during the compression stroke consists of fuel, air, and residual gases. A cycle simulation, assuming complete combustion, determines the amount and composition of residual gas. During combustion, the change from initial mixture to combustion products is assumed to be proportional to the Vibe combustion profile with an assumed start and end of combustion determined using a two-step iterative process [34]: (1) after ROHR is calculated, the new start and end of combustion is calculated and compared with the assumed values and (2) if both of them are equal the iteration is completed. The in-cylinder temperature is calculated using the ideal gas equation and calculated mass, volume, and composition profiles during the closed portion of the cycle.

Continuous exhaust emissions sampling occurs at the exhaust manifold attached to cylinder 4, directly before where the exhaust converges with that of the other cylinders. The gas analyzer system (Horiba) includes separate analyzers to determine concentrations of unburned hydrocarbons (flame ionization), oxygen (magnetopneumatic), carbon monoxide (infrared), carbon dioxide (infrared), and nitric oxides (chemiluminescent). The results are reported as dry concentrations, as water is condensed out of the exhaust samples before the gas analyzer. The emissions data is used to accurately compute the equivalence ratio in post-processing [35].

2.4. Experimental procedure

Using the experimental apparatus described above, experiments were conducted across a range of equivalence ratios (0.08, 0.20, 0.30) at an intake pressure of 1.8 bar (absolute) using a number of additive-in-ethanol combinations as fuel. Concentrations of 100, 200 and 400 mg/L of metal acetate-in-ethanol are investigated, and results are compared with naturally aspirated conditions. The mass concentrations of each additive are presented as molar concentrations in the following figures. Ethanol is selected as the base fuel because of its higher solubility of metal acetates when compared to gasoline. An ion signal-to-noise ratio (SNR) is computed to compare the signal strength against background noise to accommodate comparison with the different fuel additives. The ion circuitry outputs a filtered ion voltage to a data logging system (National Instruments LabView) to compute the SNR using the root-mean-squared of the signal noise during non-combustion portions of the thermodynamic cycle.

2.5. Experimental uncertainties

The in-cylinder pressure and ion signals are averaged over 300 consecutive cycles. Cycle-to-cycle variation of the in-cylinder pressure signals was 1% while the cycle-to-cycle variation of peak ion signals was 20%. The larger ion signal variations are a consequence of the local measurement inside the chamber, whereas the pressure signal is averaged. Combustion timing, as defined by CA50, remained constant at an average of 2.5° ± 0.25° ATDC for all test conditions. Small variations in emissions data (6% for NO_x, <2% for other emissions) affect the calculated equivalence ratio by less than 5%. These variations decreased at the higher equivalence ratios.

2.6. Numerical model procedure

Insight into the alkali metal ionization processes occurring inside the combustion chamber can be gained by simulating the HCCI combustion process. A highly idealized, single-zone model that is spatially uniform with time-dependent chemical composition, temperature, and pressure is modeled using an in-house Well-Mixed Reactor (WMR) code, which includes Woschni heat transfer equations [34]. A slider-crank relation is used to determine the reactor volume during the closed part of the combustion cycle. The detailed ethanol mechanism from Lawrence Livermore National Laboratory (LLNL) [36] is augmented by adding an ion mechanism (9 ionic species and 34 reactions) [37–41] for use in the simulations. Mechanisms by Benilov et al. [42] and Husain et al. [43,44] are used for the potassium and cesium oxidation processes, respectively.

The ionization processes are optimized based on Ashton and Hayhurst [45]. In the simulation, KOH and CsOH are treated as the additives instead of the metal acetates based on work by Zamansky et al. [46], who reported that alkali metal salts can decompose into their vapor hydroxide in a very short time. For example, the decomposition time from Na_2CO_3 to NaOH is 0.5 ms at a temperature of 1800 K [46]; for experiments in this study, the piston speed at 1800 rpm is 16.5 ms/stroke, so there is sufficient time for metal acetates to decompose. In the numerical model, the charge temperature at intake valve closing was adjusted to maintain a 2.5° ATDC CA50 at 1800 RPM. Additionally, the compression ratio in the model was adjusted to compensate for blow-by gas for compression phase agreement. Experimental data was used to then validate the numerical models.

2.7. Numerical model chemistry

Two 5-step models were used to model the potassium and cesium oxidation process [42–44], as shown in Tables 2 and 3. The tables include parameters for both the forward and reverse

Table 2
Potassium reaction pathways.

Step	Reaction	A (cm mol s)	b	E_a (cal/mol)
1	$K + O_2 + M \rightarrow KO_2 + M$	4.28E+23	−2.7	0.0
	$KO_2 + M \rightarrow K + O_2 + M$	2.06E+26	0.5	59034.0
2	$K + OH + M \rightarrow KOH + M$	4.32E+22	−2	0.0
	$KOH + M \rightarrow K + OH + M$	1.75E+26	−3	84366.0
3	$KOH + H \rightarrow K + H_2O$	2.21E+12	0.5	0.0
	$K + H_2O \rightarrow KOH + H$	2.01E+09	0.5	33713.0
4	$KO_2 + H \rightarrow KO + OH$	2.11E+11	0.5	0.0
	$KO + OH \rightarrow KO_2 + H$	8.83E+15	0.5	11196.0
5	$KO + H_2O \rightarrow KOH + OH$	5.95E+11	0.5	0.0
	$KOH + OH \rightarrow KO + H_2O$	1.72E+14	0.5	3026.8

Table 3
Cesium reaction pathways.

Step	Reaction	A (cm mol s)	b	E_a (cal/mol)
1	$Cs + O_2 + M \rightarrow CsO_2 + M$	3.16E+24	2.2	490.0
	$CsO_2 + M \rightarrow Cs + O_2 + M$	7.17E+13	0.5	44500.0
2	$Cs + OH + M \rightarrow CsOH + M$	1.02E+22	1.66	0.0
	$CsOH + M \rightarrow Cs + OH + M$	3.73E+26	−3	90000.0
3	$CsOH + H \rightarrow Cs + H_2O$	2.21E+12	0.5	0.0
	$Cs + H_2O \rightarrow CsOH + H$	3.70E+13	0.5	35700.0
4	$CsO_2 + H \rightarrow CsO + OH$	2.21E+12	0.5	0.0
	$CsO + OH \rightarrow CsO_2 + H$	2.00E+14	0.5	10300.0
5	$CsO + H_2O \rightarrow CsOH + OH$	5.95E+11	0.5	0.0
	$CsOH + OH \rightarrow CsO + H_2O$	5.03E+11	0.5	5320.0

reactions. The reaction rate (k) is calculated using Eq. (3), where A, b, and E_a are empirical parameters.

$$k = AT^b \exp\left(-\frac{E_a}{RT}\right) \quad (3)$$

The ionization mechanisms were used to determine the rate of electron production. While Eq. (1) is the dominant mechanism for electron production in pure ethanol, the optimized potassium and cesium ionization mechanisms are listed in Table 4 [45]. The numerical model was adjusted to determine the Arrhenius coefficient.

3. Results and discussion

3.1. Effect of boost pressure and fuel additive concentration on ion signal-to-noise ratio

Figs. 3 and 4 show the influence of boosted intake pressure on the ion signal as characterized by the SNR for CsOAc and KOAc additives, respectively. In each figure, naturally aspirated results are included as dashed lines for comparison. Data marker shapes indicate a change in equivalence ratio. The SNR increases as the concentration of each fuel additive concentration is increased. Additionally, as the equivalence ratio is increased, the ion signal strength also increases. Furthermore, the ion signal is decreased with an increase in boost pressure. At extremely lean conditions (ϕ = 0.08), the ion signal is nearly indistinguishable from the noise even at high concentrations of metal acetate additives.

As the intake pressure is increased, the SNR for each additive across all equivalence ratios decreases. This can be attributed to a decrease in in-cylinder temperature, enhanced radical recombination [47], and a higher resistance across the sensor gap between electrodes. The in-cylinder temperature affects the reaction rate related to ionization and electron density as described in Eqs. (2) and (3).

Consistent with previous findings, the CsOAc additive produced a larger increase in SNR when compared to KOAc. Fig. 5 compares the SNR for each additive across all equivalence ratios. Higher equivalence ratios increase the in-cylinder temperature and the free radical concentration, which both yield increased ionization and thus stronger ion signals. The trend between CsOAc and KOAc SNR's is attributed to the different ionization potentials. Since cesium has the lowest ionization potential, less energy is needed for ionization; this results in increased electron concentrations. Higher electron concentrations produce stronger ion currents that are then measured by the sparkplug ion sensor.

Table 4
Optimized ionization mechanism for K and Cs.

Reaction	A (cm mol s)	b	E_a (cal/mol)
$K + M = K^+ + e^- + M$	3.10E+15	0.5	100110
$Cs + M = Cs^+ + e^- + M$	3.10E+15	0.5	71000

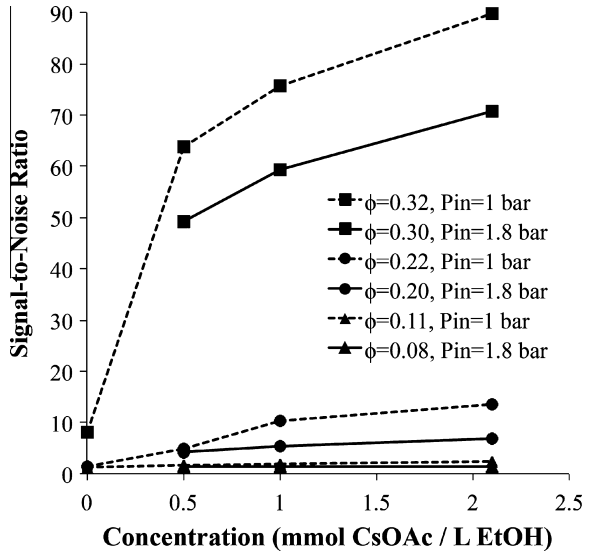

Fig. 3. Signal-to-noise ratio (SNR) versus CsOAc molar concentration at intake pressures of 1.0 and 1.8 bar.

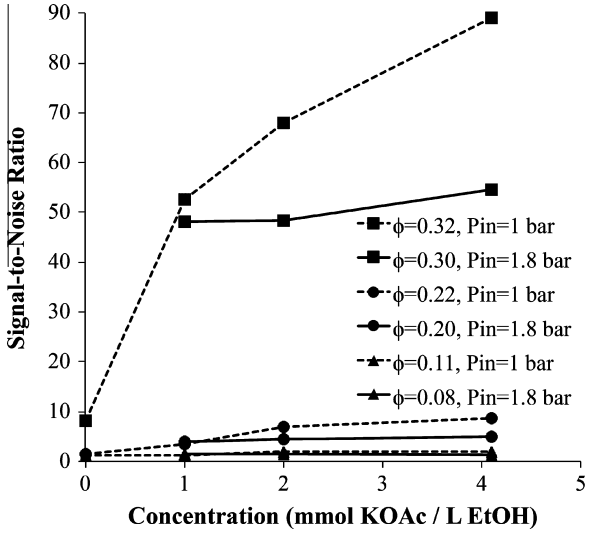

Fig. 4. Signal-to-noise ratio (SNR) versus KOAc molar concentration at intake pressures of 1.0 and 1.8 bar.

The SNR appears to reach a maximum value for each equivalence ratio, as improvements diminish with increasing concentrations. This asymptotic behavior has also been observed in previous studies [29]. CsOAc shows a high SNR-to-concentration sensitivity at lower concentrations and SNR improvements decrease with incremental increases in concentration. KOAc follows a similar trend, though with a lower sensitivity at low concentrations.

As the additive concentration is increased, the diminished return seen in ion enhancement is related to the in-cylinder temperature, which can be calculated using Woschni's correlation [34]. Fig. 6 shows that as the additive concentration is increased, the maximum in-cylinder temperature slightly decreases. This reduction in in-cylinder temperature affects the ionization process of the metal acetates. Correspondingly, a threshold exists at which additional metal acetates begin to reduce the in-cylinder tempera-

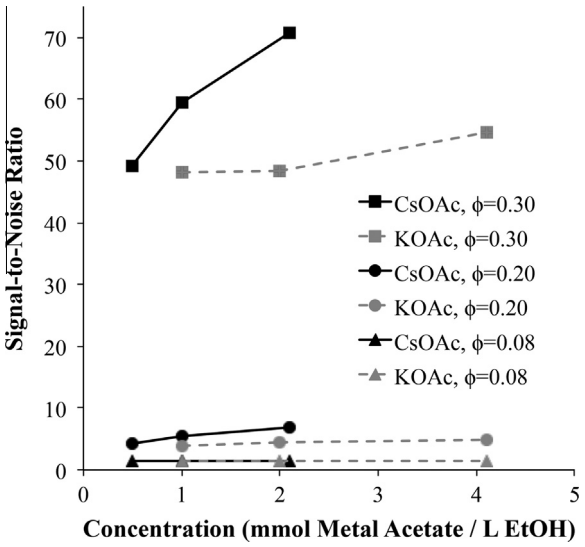

Fig. 5. Signal-to-noise ratio versus molar concentration of CsOAc and KOAc at an intake pressure of 1.8 bar.

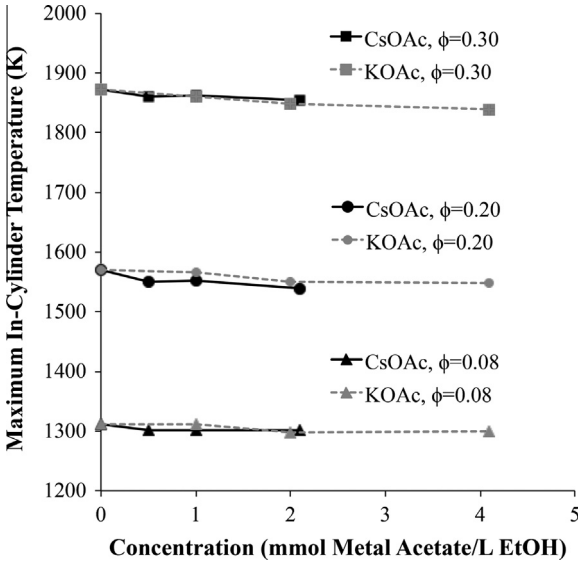

Fig. 6. Maximum in-cylinder temperature versus CsOAc and KOAc molar concentrations at equivalence ratios of 0.08, 0.20, and 0.30. Intake pressure is 1.8 bar.

ture to a level where no additional ion signal benefits are observed [29].

3.2. Effect of fuel additive concentration on pressure trace and ion signal

As shown in Fig. 3, an increase in the metal acetate concentration and equivalence ratio corresponds to an increase in SNR. Figs. 7–10 display the pressure and ion current traces at equivalence ratios 0.20 and 0.30 for CsOAc and KOAc additives. At ϕ = 0.08, ion signals are nearly indistinguishable, thus those plots are not presented here. The primary vertical axis (pressure) scaling is held constant for each figure; however, the secondary *y*-axis (ion current) is scaled from 0 to 1 for ϕ = 0.20 and 0 to 10 for ϕ = 0.30 for clarity.

Increasing the equivalence ratio produces stronger, more distinguishable ion signals. The CsOAc additive produces more

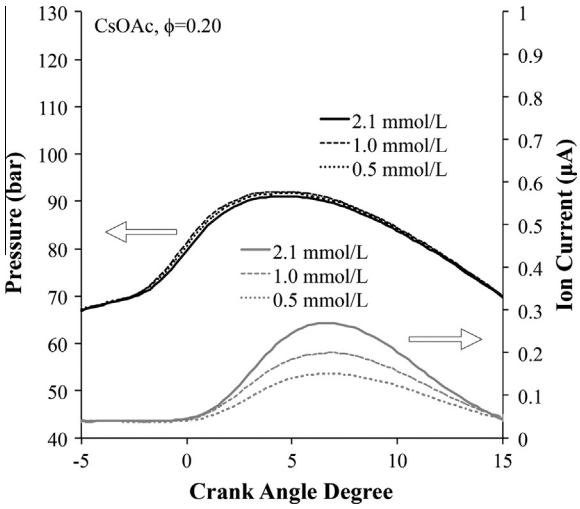

Fig. 7. CsOAc pressure and ion current traces at ϕ = 0.20.

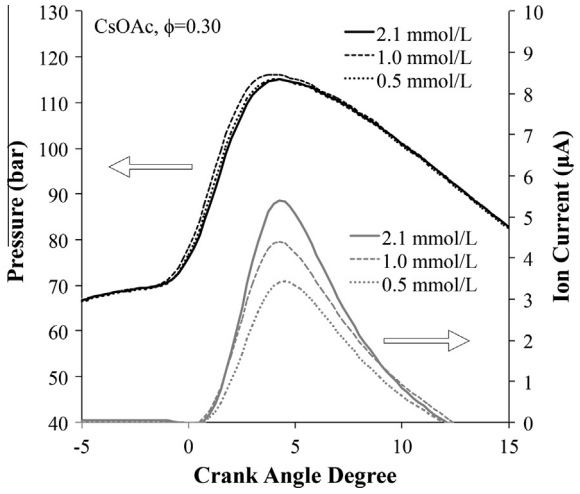

Fig. 8. CsOAc pressure and ion current traces at ϕ = 0.30.

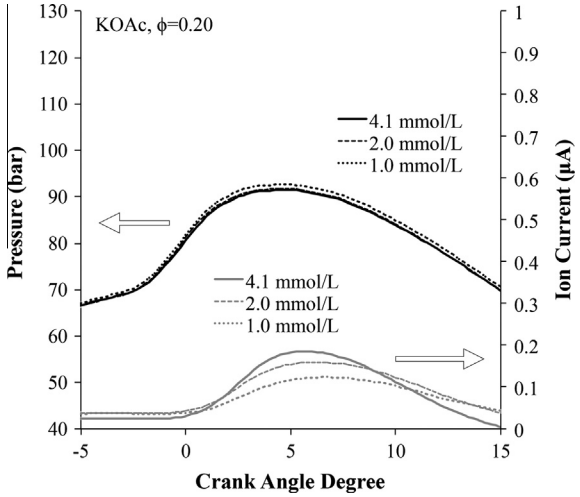

Fig. 9. KOAc pressure and ion current traces at ϕ = 0.20.

distinguishable ion signals for every concentration when compared to KOAc. A slight decrease in cylinder pressure is observed with increasing additive concentration. Metal acetates inhibit flame

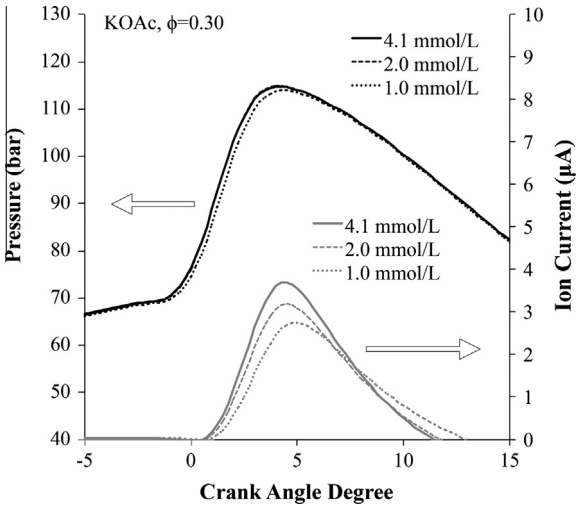

Fig. 10. KOAc pressure and ion current traces at $\phi = 0.30$.

development through reductions in maximum temperature, OH radical production, and flame speed [48–50].

The decrease in in-cylinder pressure results in a lower gross indicated mean effective pressure ($IMEP_g$) for increased concentrations. Changes in $IMEP_g$ were nearly equivalent for each additive as the concentration is varied from 0 to 400 mg/L. At $\phi = 0.30$, $IMEP_g$ decreases from 5.73 bar to 5.53 bar. At $\phi = 0.20$, $IMEP_g$ decreases from 3.47 bar to 3.16 bar. At $\phi = 0.08$, $IMEP_g$ decreases from 0.89 bar to 0.71 bar.

3.3. Effect of fuel additive concentration on heat release rate

As the additive concentration is increased, the maximum rate of heat release (ROHR) decreases. This effect is a function of the corresponding decreases in in-cylinder pressure and temperature. Fig. 11 shows the maximum ROHR for a range of additive concentrations at equivalence ratios of 0.30, 0.20, and 0.08. As expected, higher equivalence ratios produce the largest maximum ROHR; an increase in metal acetate concentration lowers the maximum ROHR at each equivalence ratio. At $\phi = 0.30$, the observed reduction is ~4%. For $\phi = 0.20$, the reduction in maximum ROHR is approximately 4.5%. The largest effect is seen at the lowest equivalence ratio ($\phi = 0.08$) where the decrease in ROHR is ~4.7%. The reduction in maximum ROHR is evident even at the lowest additive concentrations.

The engine experiments maintained a constant combustion timing of 2.5° after top-dead-center (ATDC), as defined by the crank angle degree (CAD) where 50% of the cumulative heat release occurs (CA50). Combustion timing was maintained using the apparatus described in Section 2.1 with a variation of <0.25 CAD. Fig. 12 shows that the intake temperature (T_{in}) remains relatively constant across the range of additive concentrations. The higher equivalence ratios, $\phi = 0.20$ and $\phi = 0.30$, experience a slight rise in T_{in} (a maximum 0.6% and 3%, respectively). Thus, the maximum ROHR reduction can be attributed to the metal acetate addition rather than changes in intake temperature. At the lowest equivalence ratio

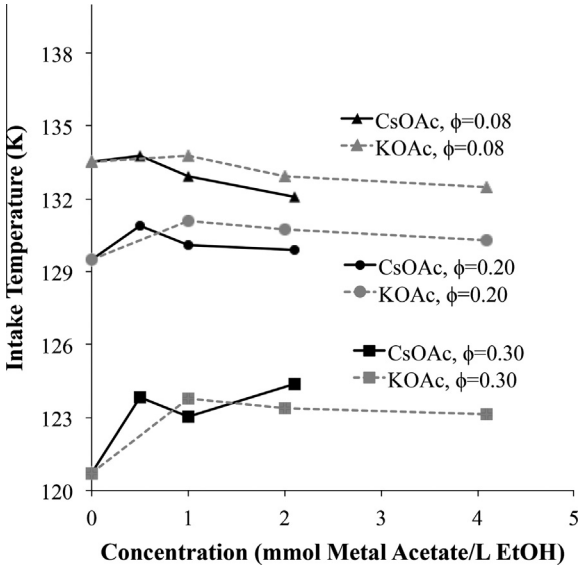

Fig. 12. Intake temperature versus CsOAc and KOAc molar concentrations at equivalence ratios of 0.08, 0.20, and 0.30.

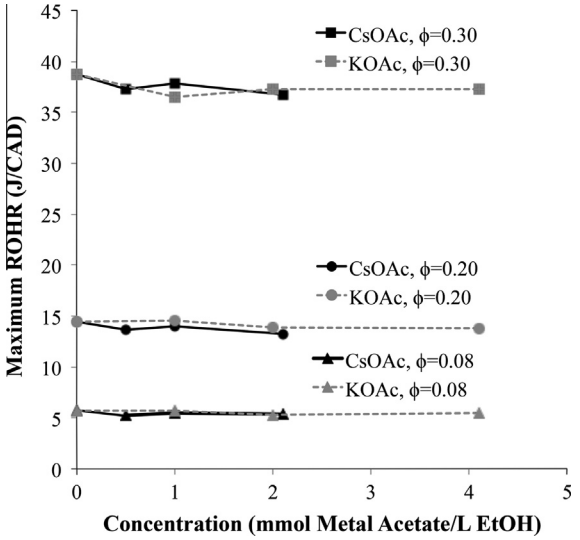

Fig. 11. Maximum rate of heat release (ROHR) versus CsOAc and KOAc molar concentrations at equivalence ratios of 0.08, 0.20, and 0.30.

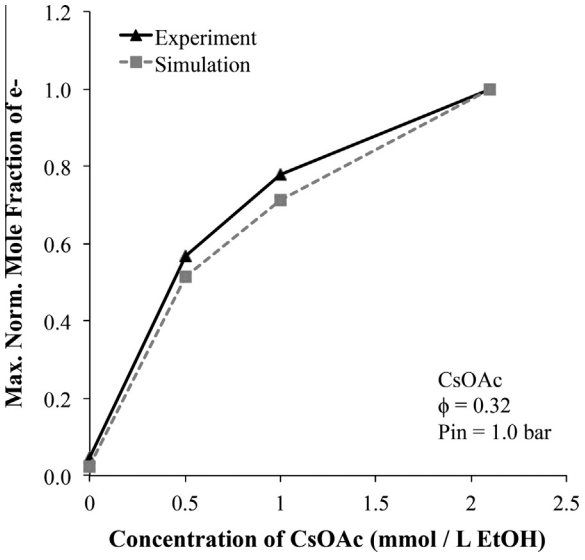

Fig. 13. Normalized maximum values of ion current traces of experimental data and numerical model over a range of CsOAc concentrations; $\phi = 0.32$ and $P_{in} = 1.0$ bar.

(ϕ = 0.08), a slight reduction in T_{in} is observed at a maximum level of 1.1%.

These trends are consistent when compared to naturally aspirated conditions [28]. As a result of the higher intake pressures presented here, the required T_{in} and maximum ROHR values are higher when compared to the naturally aspirated results.

3.4. CsOAc numerical modeling

Fig. 13 shows a comparison between the cesium ionization numerical model and experimental results. The numerical model was validated using the experimental results at ϕ = 0.32 over a range of CsOAc concentrations at an intake pressure of 1.0 bar. The constants A = 3.1E + 15 cm mol s, b = 0.5, and E_a = 7.1E + 04 cal/mol were used for the reaction rate (Eq. (3)) to fit the experimental data.

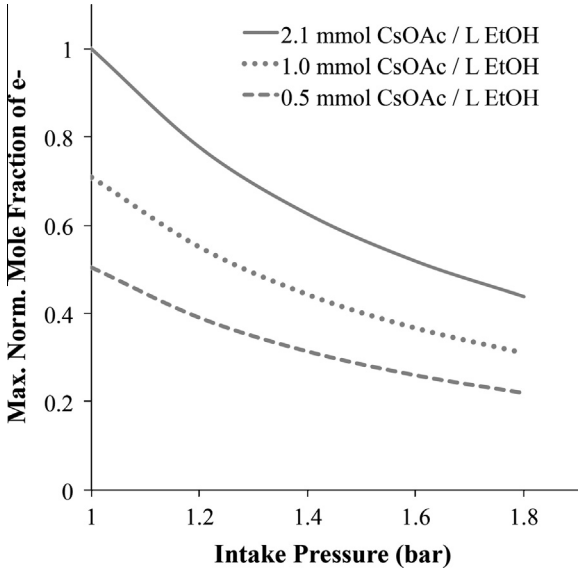

Fig. 14. Normalized maximum mole fraction of electrons over a range of intake pressures for CsOAc additive; ϕ = 0.30.

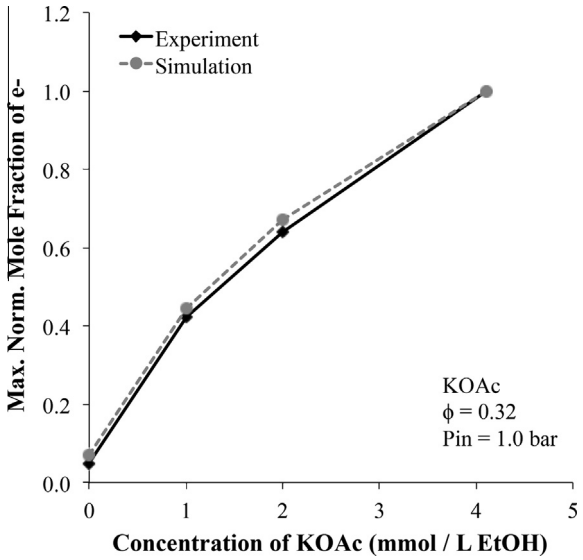

Fig. 15. Normalized maximum values of ion current traces of experimental data and numerical model over a range of KOAc concentrations; ϕ = 0.32 and P_{in} = 1.0 bar.

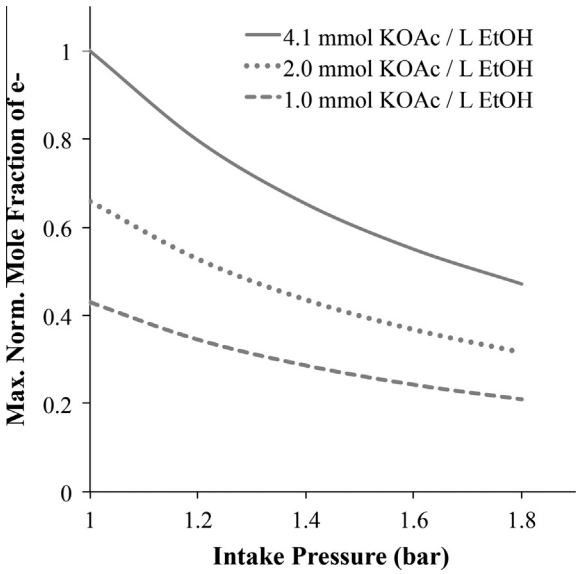

Fig. 16. Normalized maximum mole fraction of electrons over a range of intake pressures for KOAc additive; ϕ = 0.30.

After validating the maximum value of ion current trace, the cesium ionization mechanism is used to predict the ion current traces at boosted conditions at each additive concentration. In Fig. 14, the numerical model predicts the observed decrease in peak ion signals as the intake pressure is increased. The model additionally captures a decrease in ion signal with lower additive concentrations.

3.5. KOAc numerical modeling

Fig. 15 compares the normalized maximum values of normalized electron mole fraction between the potassium numerical model and experimental results. The numerical model was validated using the experimental results at ϕ = 0.32 and P_{in} = 1.0 bar. The reaction rate used constants of A = 3.1E + 15 cm mol s, b = 0.5, and E_a = 1.0011E + 5 cal/mol to fit the experimental data.

After validating the maximum value of ion current trace, the potassium ionization mechanism is used to predict the ion current traces at boosted conditions at each additive concentration. As seen in Fig. 16, the numerical model shows that an increase in intake pressure is accompanied by a reduction in the peak ion signal. The maximum normalized mole fraction of electrons decreases at a greater rate for the KOAc additive in comparison with the modeling results for CsOAc. Furthermore, a reduction in additive concentration lowers the peak ion signal.

4. Conclusions

Two different metal acetates (CsOAc and KOAc) were used as additives to ethanol in a homogeneous charge compression ignition (HCCI) engine. The experiments show each additive produces an increased ion signal-to-noise ratio (SNR), as detected using a sparkplug ion sensor. The ion signal is more apparent at higher equivalence ratios (ϕ = 0.20 and ϕ = 0.30) and nearly indistinguishable at ϕ = 0.08. An increase in intake pressure produces a decrease in the ion signal, primarily attributed to a decrease in the in-cylinder temperature. The CsOAc additive produced the strongest ion signal enhancement than the KOAc additive across all operating conditions. The use of metal acetates as additives yielded reductions in the gross indicated mean effective pressure ($IMEP_g$) and the maximum rate of heat release (ROHR). A single-zone

numerical model was able to predict the peak ion signal, combustion timing, and intake pressure dependence for both cesium and potassium ionization chemistry.

Acknowledgements

This study was supported by LLNL under award number B586434 (Low Temperature Combustion Chemistry at Boost Pressures for Surrogate Fuels and Ethanol Use in HCCI Engine Experiments). The KOAc additive for this study was provided by T.S. Lee at the Joint BioEnergy Institute (JBEI) led by Lawrence Berkeley National Laboratory (LBNL). Additional thanks to Jacob Cross, Franciel Gusberti, Samveg Saxena, Darko Kozarac, David Vuilleumier, Daniel Schuler, Tung Phan, and Aditya Desai for their contributions.

References

[1] Warnatz J, Maas U, Dibble RW. Combustion: physical and chemical fundamentals, modeling and simulation, experiments, pollutant formation. 4th ed. Springer; 2006.
[2] Epping K, Aceves S, Bechtold R, Dec J. The potential of HCCI combustion for high efficiency and low emissions. SAE technical paper 2002-01-1923; 2002.
[3] Xiea H, Lia L, Chena T, Zhao H. Investigation on gasoline homogeneous charge compression ignition (HCCI) combustion implemented by residual gas trapping combined with intake preheating through waste heat recovery. Energy Convers Manage 2014;86:8–19.
[4] Gray AW, Ryan TW. Homogeneous Charge Compression Ignition (HCCI) of diesel fuel. SAE technical paper 971676; 1997.
[5] Christensen M, Johansson B, Einewall P. Homogeneous Charge Compression Ignition (HCCI) using isooctane, ethanol and natural gas - a comparison with spark ignition operation. SAE technical paper 972874; 1997.
[6] Maurya RK, Agarwal AK. Experimental study of combustion and emission characteristics of ethanol fuelled port injected homogeneous charge compression ignition (HCCI) combustion engine. Appl Energy 2011;88(4):1169–80.
[7] Zheng M, Han X, Asad U, Wang J. Investigation of butanol-fuelled HCCI combustion on a high efficiency diesel engine. Energy Convers Manage 2015;98:215–24.
[8] Xingcai L, Yuchun H, Libin J, Linlin Z, Zhen H. Heat release analysis on combustion and parametric study on emissions of HCCI engines fueled with 2-propanol/n-heptane blend fuels. Energy Fuels 2006;20(5):1870–8.
[9] Saisirirat P, Togbé C, Chanchaona S, Foucher F, Mounaim-Rousselle C, Dagaut P. Auto-ignition and combustion characteristics in HCCI and JSR using 1-butanol/n-heptane and ethanol/n-heptane blends. Proc Combust Inst 2011;33(2):3007–14.
[10] Mack JH, Flowers DL, Buchholz BA, Dibble RW. The effect of the Di-Tertiary Butyl Peroxide (DTBP) additive on HCCI combustion of fuel blends of ethanol and diethyl ether. SAE technical paper 2005-01-2135; 2005.
[11] Santoso H, Matthews J, Cheng WK. Managing SI/HCCI dual-mode engine operation. SAE technical paper 2005-01-0162; 2005.
[12] Dec J, Yang Y. Boosted HCCI for high power without engine knock and with ultra-low NO_x emissions – using conventional gasoline. SAE Int J Engines 2010;3(1):750–67.
[13] Sjöberg M, Dec J, Cernansky N. Potential of thermal stratification and combustion retard for reducing pressure-rise rates in HCCI engines, based on multi-zone modeling and experiments. SAE technical paper 2005-01-0113; 2005.
[14] Krasselt J, Foster D, Ghandhi J, Herold R, Reuss D, Najt P. Investigations into the effects of thermal and compositional stratification on HCCI combustion – Part I: Metal engine results. SAE technical paper 2009-01-1105; 2009.
[15] Christensen E, Yanowitz J, Ratcliff M, McCormick RL. Renewable oxygenate blending effects on gasoline properties. Energy Fuels 2011;25:4723–33.
[16] Oakley A, Zhao H, Ladommatos N, Ma T. Experimental studies on Controlled Autoignition (CAI) combustion of gasoline in a 4-stroke engine. SAE technical paper 2001-01-1030; 2001.
[17] Yao M, Zheng Z, Liu H. Progress and recent trends in homogeneous charge compression ignition (HCCI) engines. Prog Energy Combust Sci 2009;35:398–437.
[18] Easley WL, Agarwal A, Lavoie GA. Modeling of HCCI combustion and emissions using detailed chemistry. SAE technical paper 2001-01-1029; 2001.
[19] Souder JS, Mack JH, Hedrick JK, Dibble RW. Microphones and knock sensors for feedback control of HCCI engines. ASME ICEF2004-960; 2004.
[20] Taraza D, Henein NA, Bryzik W. Determination of the gas pressure torque of a multicylinder engine from measurements of the crankshaft's speed variation. SAE technical paper 980164; 1998.
[21] Auzins J, Johansson H, Nytomt J. Ion-gap sense in misfire detection, knock and engine control. SAE technical paper 950004; 1995.
[22] Reinmann R, Saitzkoff A, Mauss F. In-cylinder pressure measurement using the spark plug as an ionization sensor. SAE technical paper 970857; 1997.
[23] Fan Q, Bian J, Lu H, Tong S, Li L. Misfire detection and re-ignition control by ion current signal feedback during cold start in two-stage direct-injection engines. Int J Eng Res 2012;15(1):37–47.
[24] Strandh P, Christensen M, Bengtsson J, Johansson R, Vressner A, Tunestal P, Johansson B. Ion current sensing for HCCI combustion feedback. SAE technical paper 2003-01-3216; 2003.
[25] Celements RM, Smy PR. The variation of ionization with air/fuel ratio for a spark ignition engine. J Appl Phys 1976;47(2).
[26] Bogin GE, Mack JH, Dibble RW. Spark plug modifications for improving ion sensing capabilities in a Homogeneous Charge Compression Ignition (HCCI) engine. In: Proceedings of the ASME ICE spring conference, ICES2009-76161; 2009.
[27] Bogin G, Mack JH, Dibble RW. Fuel effects of ion sensing in a homogeneous charge compression ignition (HCCI) engine. June 2009, SAE technical paper 2009-01-1805; 2009.
[28] Chen Y, Li L, Miao Q, Cao Y, Liu Y, Liu Z, Deng J. Effect of stratification on ion distribution in HCCI combustion using 3D-CFD with detailed chemistry. SAE technical paper 2013-01-2512; 2013.
[29] Butt RH, Chen Y, Mack JH, Saxena S, Dibble RW, Chen JY. Improving ion current of sparkplug ion sensors in HCCI combustion using sodium, potassium, and cesium acetates: experimental and numerical modeling. In: Proceedings of the combustion institute, vol. 35(3); 2015.
[30] Lide DR, editor. Handbook of chemistry and physics. CRC Press; 1992. p. 10–211.
[31] Vuilleumier D, Selim H, Dibble RW, Sarathy M. Exploration of heat release in a homogeneous charge compression ignition engine with primary reference fuels. SAE technical paper 2013-01-2622; 2013.
[32] Savitzky A, Golay MJE. Smoothing and differentiation of data by simplified least squares procedures. Anal Chem 1964;36:1627–39.
[33] Heywood JB. Internal combustion engine fundamentals. McGraw-Hill series in mechanical engineering. New York: McGraw-Hill; 1988.
[34] Woschni G. A universally applicable equation for the instantaneous heat transfer coefficient in the internal combustion engine. SAE technical paper 670931; 1967.
[35] Chan SH, Zhu J. Exhaust emission based air-fuel ratio model (I): literature reviews and modelling. SAE technical paper 961020; 1996.
[36] Marinov NM. A detailed chemical kinetic model for high temperature ethanol oxidation. Int J Chem Kinet 1999;31:183–220.
[37] Calcote HF, Gill RJ. Development of the kinetics for an ionic mechanism of soot formation in flames. Eastern States Section of the Combustion Institute, Fall Technical Meeting; 1994.
[38] Brown RC, Eraslan AN. Simulation of ionic structure in lean and close-to-stoichiometric acetylene flames. Combust Flame 1988;73(1):1–21.
[39] Rowe BR, Gomet JC, Canosa A, Rebrion C, Mitchell JBA. A further study of HCO^+ dissociative recombination. J Chem Phys 1992;96(2):1105–10.
[40] Guo J, Goodings JM. Recombination coefficients for H_3O^+ ions with electrons e^- and with Cl^-, Br^- and I^- at flame temperatures 1820–2400 K. Chem Phys Lett 2000;329(5 and 6):393–8.
[41] Mehresh P, Souder J, Flowers D, Riedel U, Dibble RW. Combustion timing in HCCI engines determined by ion-sensor: experimental and kinetic modeling. Combust Inst 2005;30:2701–9.
[42] Benilov MS, Pozdeev PA, Rogov BV, Sinel'shchikov VA. Nonequilibrium boundary layer of potassium-seeded combustion products. Combust Flame 1994;98(4):313–25.
[43] Husain D, Ji B. Determination of the absolute third-order rate constant for reaction between Cs + O_2 + N_2 by time-resolved atomic resonance absorption spectroscopy. J Photochem Photobiol A: Chem 1990;53(2):169–80.
[44] Husain D, Plane JMC, Xiang CC. Measurement of the absolute third-order rate constant for the reaction between Cs + OH + He determined by time-resolved molecular resonance-fluorescence spectroscopy, OH($A^2\Sigma^+$–$X^2\Pi$), coupled with steady atomic resonance fluorescence, Cs(7^2P_J–$6^2S_{1/2}$). J Chem Soc, Faraday Trans 2 1985;81:769–82.
[45] Ashton AF, Hayhurst AN. Kinetics of collisional ionization of alkali metal atoms and recombination of electrons with alkali metal ions in flames. Combust Flame 1973;21(1):69–75.
[46] Zamansky VM, Maly PM, Ho L, Lissianski VV, Rusli D, Gardiner WC. Promotion of selective non-catalytic reduction of no by sodium carbonate. Symp (Int) Combust 1998;27(1):1443–9.
[47] Lawton J, Weinberg FJ. Electrical aspects of combustion. Oxford: Clarendon Press; 1965.
[48] Jensen DE, Jones GA. Theoretical aspects of secondary combustion in rocket exhausts. Combust Flame 1981;41:71–85.
[49] Day MJ, Stamp DV, Thompson K, Dixon-Lewis G. Inhibition of hydrogen-air and hydrogennitrous oxide flames by halogen compounds. Proc Combust Inst 1971;13:705–12.
[50] Rosser WA, Inami SH, Wise H. The effect of metal salts on premixed hydrocarbon—air flames. Combust Flame 1963;7:107–19.